The Effect of Sc and Zr Additions on the Structure, Mechanical, and Corrosion Properties of a High Thermal Conductive Al–3%Zn–3%Ca Alloy

Anastasia Lyskovich , Viacheslav Bazhenov * , Ivan Baranov , Mikhail Gorshenkov , Olga Voropaeva , Andrey Stepashkin , Vitaliy Doroshenko , Ruslan Yu. Barkov , Shevket Rustemov , Andrey Koltygin

Posted Date: 10 December 2025

doi: 10.20944/preprints202512.0932.v1

Keywords: aluminum alloys; thermal conductivity; phase composition; Sc addition; Zr addition; heat treatment; tensile test; corrosion resistance

 doi:10.20944/preprints202512.0932.v1

Article

The Effect of Sc and Zr Additions on the Structure, Mechanical, and Corrosion Properties of a High Thermal Conductive Al–3%Zn–3%Ca Alloy

Anastasia Lyskovich [1], Viacheslav Bazhenov [1,*], Ivan Baranov [1], Mikhail Gorshenkov [2], Olga Voropaeva [3], Andrey Stepashkin [4], Vitaliy Doroshenko [5], Ruslan Barkov [6], Shevket Rustemov [1] and Andrey Koltygin [1]

[1] Casting Department, National University of Science and Technology "MISIS", Leninskiy pr. 4, 119049 Moscow, Russia
[2] Physical Materials Science Department, National University of Science and Technology "MISIS", Moscow, Leninskiy pr. 4, 119049 Moscow, Russia
[3] Departament of Metallurgy Steel, New Production Technologies and Protection of Metals, National University of Science and Technology "MISIS", Leninskiy pr. 4, 119049 Moscow, Russia
[4] Center of Composite Materials, National University of Science and Technology "MISIS", Leninskiy pr. 4, 119049 Moscow, Russia
[5] Department of Metal Forming, National University of Science and Technology "MISIS", Leninskiy pr. 4, 119049 Moscow, Russia
[6] Department of Physical Metallurgy of Non-Ferrous Metals, National University of Science and Technology "MISIS", Leninskiy pr. 4, 119049, Moscow, Russia
* Correspondence: v.e.bagenov@gmail.com; Tel.: +7-(905)-553-55-64

Abstract

Al–Zn–Ca alloys are good candidates for industrial electronics and electric vehicles due to their high thermal conductivity, castability, and corrosion resistance, but their strength requires improvement. This study investigates how Sc and Zr additions affect the microstructure, thermal, mechanical, and corrosion properties of an Al–3wt%Zn–3wt%Ca base alloy. Microstructural analysis showed that substituting Sc with Zr did not drastically alter the phase composition but changed the elemental distribution: Sc was uniform, while Zr segregated to dendritic cores. Zr addition also refined the grain size from 488 to 338 μm. An optimal aging treatment at 300 °C for 3 hours was established, which enhanced hardness for all alloys via precipitation of Al_3Sc/Al_3(Sc,Zr) particles. However, this Zr substitution reduced thermal conductivity (from 184.7 to 168.0 W/mK) and ultimate tensile strength (from 269 to 206 MPa), though it improved elongation at fracture (from 4.6 to 7.1%). All aged alloys exhibited high corrosion resistance in 5.7% NaCl + 0.3% H_2O_2 solution, with Zr-containing variants showing a lower corrosion rate and better pitting resistance. The study confirms the potential of tuning Sc/Zr ratios in Al–Zn–Ca alloys to achieve a favorable balance of strength, ductility, thermal conductivity, and corrosion resistance.

Keywords: aluminum alloys; thermal conductivity; phase composition; Sc addition; Zr addition; heat treatment; tensile test; corrosion resistance

1. Introduction

In the context of a growing demand for electrical appliances and electric vehicles, the necessity for effective heat sinks is increasing. These devices are tasked with maintaining optimal heat dissipation during operation to prevent overheating. The materials used in the construction of contemporary cooling heat sinks must exhibit high thermal conductivity in order to facilitate rapid and uniform heat transfer, thereby ensuring the optimal operation of electrical equipment [1]. In the

 doi:10.20944/preprints202512.0932.v1

development of a highly thermally conductive aluminum alloy, great care is taken to ensure an optimal combination of thermal conductivity and mechanical properties.

In order to meet the requirements of modern heat sinks, it is necessary for them to combine low weight with high heat dissipation capacity. The following design solutions are employed in the creation of heat sinks: i) the number of fins is typically augmented to enhance thermal regulation efficiency; ii) the product's weight is reduced by reducing the thickness of the fins and the base of the heat sink [2]. In light of the intricate design of heat sinks, the predominant manufacturing technique employed for their large-scale production is die-casting [3,4].

One area of advanced research is the development of new alloys that combine high thermal conductivity and good castability [5–9]. These alloys should comprise a substantial proportion of eutectic within their structure, while exhibiting minimal solubility of the eutectic-forming element in the Al solid solution [10]. Among the promising candidates, the Al–Ca alloys is of particular interest, containing the α-Al+Al_4Ca eutectic with a very fine structure [11,12]. The Al–Ca base alloys advantage is its favorable castability [13], and the virtually negligible solubility of Ca in α-Al [14]. In the preceding study, the Al–3 wt% Zn–3 wt% Ca alloy exhibited considerable potential for utilization as a heat-conducting material for the fabrication of heat sinks through the casting technique [15]. Nevertheless, despite the alloy's high thermal conductivity (approximately 194 W/mK) and favorable castability and corrosion resistance, its tensile yield strength remained below 50 MPa. The low strength of the alloy represents a significant limitation on its potential applications.

One of the most effective methods for enhancing the mechanical properties of aluminum alloys is the alloying with rare earth elements, with Sc being the most efficacious [16,17]. During the solidification of Al–Sc alloys, Al_3Sc particles are precipitated, which have a face-centered cubic lattice of the $L1_2$ type [18]. These particles serve as nucleation sites in the aluminum melt during solidification, thereby contributing to grain refinement [19–21]. The precipitates of the Al_3Sc phase formed during heat treatment, serves as a strong hardener of aluminum alloys [18]. Nevertheless, the high cost of Sc makes its use in alloys for large scale production of castings challenging. Consequently, in order to reduce the cost of the material, Sc is frequently employed in conjunction with Zr. During the solidification of Al–Sc–Zr alloys, not only primary Al_3Sc crystals but also $Al_3(Sc,Zr)$ crystals, which also have an $L1_2$ structure participated [22,23]. Furthermore, nanosized $Al_3(Sc,Zr)$ precipitates markedly impede the movement of dislocations and grain boundaries, thereby enhancing the strength of the alloy [24]. Accordingly, the addition of Sc and Zr may facilitate the attainment of superior mechanical properties in the promising Al–3 wt% Zn–3 wt% Ca aluminum alloy.

The objective of the study is to ascertain the effect of the Sc and Zr ratio in the Al–3 wt% Zn–3 wt% Ca alloy on the mechanical properties, corrosion properties, and thermal conductivity; and to determine the optimal heat treatment regime for mentioned alloys.

2. Materials and Methods

Four Al–3 wt% Zn–3 wt% Ca–Sc–Zr alloys with different Sc/Zr ratio were prepared. The melting was carried out in clay-graphite crucible using a high-frequency induction furnace. The following master alloys and pure metals were used: Al (99.99 wt%), Zn (99.98 wt%), Al–11 wt% Ca, Al–2 wt% Sc, Al–3 wt% Zr. After the alloy was completely melted the C_2Cl_6 was employed to degassing at melt temperature of 740 °C. Next the melt was cooled down to reach the temperature of 720 °C and was poured into the permanent steel and graphite molds. The specimens for structural analysis and tensile testing were cut from the 32 × 340 × 50 mm^3 ingots produced in the graphite mold. The specimens for hardness measurements, thermal conductivity evaluation, and corrosion resistance were cut from the ⌀35 × 150 mm ingots obtained in the steel mold.

The equilibrium (Lever rule) and non-equilibrium (Scheil-Gulliver solidification model [25]) solidification process of Al–Zn–Ca–Sc–Zr alloys and precipitation kinetics of Al_3Sc/$Al_3(Sc,Zr)$ was calculated using the Thermo-Calc Software with the TTAL5 and MOBAL1 databases, which provide thermodynamic and kinetic data respectively [26].

 doi:10.20944/preprints202512.0932.v1

The microstructures of the alloys and the alloys composition were investigated using energy-dispersive X-ray spectroscopy (EDS) on a Tescan Vega SBH3 scanning electron microscope (SEM) with an Oxford EDS detector. The as-cast alloys compositions are summarized in Table 1. Four specimens (20 × 30 × 10 mm^3), one for each alloy were ground and polished for metallographic observations. The polished specimens were anodized in Barker's solution (10% HBF_4 water solution) according to the following regime: current density 0.1 A/cm^2; voltage: 25 V; exposure time 30–60 s. The average grain size was measured using the linear-intercept method. To analyze the average grain size, at least 3 images of the macrostructure were taken in different parts of the sample.

The samples for transmission electron microscopy (TEM) were subjected to mechanical grinding, resulting in a thickness of approximately 300 μm. Next, the foils for TEM were prepared by double-jet electropolishing in HNO_3–CH_3OH (1:4 volume fractions) electrolyte held at –20 °C using STRUERS TenuPol 5 polishing machine. TEM observations were done using bright-field, dark-field imagining, and select-area electron diffraction with the help of JEOL JEM1400 transmission electron microscope operating at 120 kV. The sizes of the precipitates are determined using ImageJ software (version 1.52a, National Institutes of Health, USA) on the dark-field TEM images. Each average value of the precipitate diameter is deduced from a measurement of more than 400 precipitates.

Table 1. Chemical compositions of investigated alloys.

Alloy		Element Content (wt%)				
		Al	Zn	Ca	Sc	Zr
#1	AlZn3Ca3Sc0.3	Bal.	3.09	2.87	0.32	–
#2	AlZn3Ca3Sc0.2Zr0.05	Bal.	3.13	2.99	0.20	0.06
#3	AlZn3Ca3Sc0.2Zr0.1	Bal.	3.09	2.82	0.17	0.11
#4	AlZn3Ca3Sc0.1Zr0.2	Bal.	3.29	2.93	0.12	0.23

The as-cast alloys were aged at 200–400 °C from 3 to 24 h. The effect of aging treatment on alloys was evaluated by analysis of hardness and thermal conductivity. The specimens, measuring 20 × 10 × 10 mm^3 were then grounded using P400 grit SiC abrasive paper. Brinell hardness was measured using an INNOVATEST Nemesis 9001 (Netherlands) universal hardness tester with following parameters: a ball with a diameter of 2.5 mm, an applied load of 62.5 kgf (≈ 613 N), dwelling time of 10 s. Average hardness results were obtained from 5 repeated measurements.

To estimate the thermal conductivity, the Smith and Palmer equation was used, which establishes the correlation between thermal conductivity (λ) and electrical conductivity (σ) in alloys, specifically, aluminum alloys (without silicon) [27]. Poirier and McBride [28] confirmed the high degree of agreement between the results of the calculation method for determining thermal conductivity using the Smith and Palmer equation and the measurement results. The following equation was used in this study [15]:

$$\lambda = 0.816 L_0 T \sigma + 17.94, \quad (1)$$

where L_0 is the Lorenz constant, T is the temperature. The Lorentz constant in Eq. (1) is $2.45 \cdot 10^{-8}$ $W\Omega K^{-2}$ [28]. Using a contact-free eddy current conductivity meter VE-27NC (Sigma, Russian Federation) with a measurement range of 5.0–37.0 MS/m, the σ was measured at room temperature. Generally, 10 measurements were performed to evaluate the average σ value for each specimen. Next, the thermal conductivity was calculated using Eq. (1).

Additionally, thermal conductivity was determined through the application of an alternative methodology. The variation of density (ρ) with temperature was derived through the thermal expansion coefficient, which was ascertained using a DIL 402 C dilatometer (NETZSCH, Germany). The thermal diffusivity (a) was determined using the laser flash method (LFA), with the LFA 447 apparatus (NETZSCH, Germany). The variation of heat capacity (C_p) of aluminum with temperature was calculated using the NIST JANAF equations [29]. Third-order polynomials were employed to

 doi:10.20944/preprints202512.0932.v1

model the relationship between the thermal properties and temperature. Thermal conductivity (λ) was determined using the thermal diffusivity equation:

$$\lambda = a\rho C_p \quad (2)$$

The mechanical properties of alloys after aging at 300 °C for 3 h was obtained. For tensile testing, an Instron 5569 universal testing machine (USA) with an advanced video extensometer was employed. Cylindrical specimens with a gauge diameter of 5 mm and a length of 80 mm were obtained by lathing [10]. The mean value of at least three measurements was calculated for each specimen.

Immersion corrosion testing was conducted on as aged alloys specimens (300 °C, 3 h) measuring 15×15×10 mm (surface area of approximately 10.5 cm^2) in an aqueous solution comprising of 5.7% NaCl and 0.3% H_2O_2 at 25 °C for a period of 15 days [30]. Four specimens were tested for each alloy. Prior to the commencement of the test, the specimens were ground using P600 grit SiC abrasive paper and weighed on the balance of the HR-202i model (AND, Japan). The H_2O_2 was replenished at five-day intervals to compensate its decomposition in the aqueous environment. Upon completion of the test, the corrosion products were removed by dipping the specimens into concentrated HNO_3 [31]. The specimens were then weighed again to determine the mass gain per unit surface area. Finally, the mean corrosion rate in mm/year was calculated in accordance with the ASTM standard [31].

The electrochemical test was performed in a 5.7% NaCl + 0.3% H_2O_2 solution at 25 °C using an IPC Pro MF potentiostat/galvanostat/FRA system configured in a three-electrode arrangement. The working electrodes consisted of alloy specimens with an exposed surface area of approximately 0.9 cm^2. The testing surface was mechanically ground using P2000 grit SiC abrasive paper and polished. After, all specimens were cleaned in distilled water. A platinum counter electrode and a saturated Ag/AgCl reference electrode completed the electrochemical cell. Prior to the test, the working electrode was placed in the electrolyte for 50 min to obtain a stable OCP. Potentiodynamic polarization curves were recorded by scanning from −1.6 V (cathodic region) to −0.6 V (anodic region) at a scan rate of 1 mV/s. For the electrochemical tests, each specimen was tested on three occasions to ensure the reproducibility of the data and the presentation of the average curves.

3. Results and Discussion

3.1. Effect of Sc and Zr Additions on as-Cast Structure of Al–Zn–Ca Alloys

The solidification pathways of Al–Zn–Ca–Sc–Zr alloys that calculated using Lever rule and Scheil-Gulliver solidification models are presented in Figure 1. The Scheil-Gulliver solidification calculations of the AlZn3Ca3Sc0.3 alloy indicate that, following the formation of primary α-Al crystals, an eutectic reaction, L → α-Al + $L1_2$, where $L1_2$ is Al_3Sc phases having a cubic $L1_2$-ordered crystal structure, should occur. The solidification of this alloy should be completed by the ternary eutectic reaction L → α-Al + $L1_2$ + Al_4Ca. As demonstrated in Figure 1b–d, the solidification process in alloys containing Zr, commences with the formation of primary D023 crystals, where $D0_{23}$ is Al_3(Sc,Zr) phase which has a tetragonal $D0_{23}$ crystal structure. Subsequently, in alloys containing 0.2 wt% Sc and (0.05-0.1) wt% Zr at a temperature of approximately 624 °C, the $L1_2$-Al_3(Sc,Zr) phase is precipitated from the melt in accordance with the eutectic reaction. The solidification process of these alloys culminates in the formation of a eutectic structure of $D0_{23}$ + α-Al + $L1_2$ + Al_4Ca. In the case of the as-cast alloy containing 0.1 wt% Sc and 0.2 wt% Zr, the resulting structure will consist of $D0_{23}$ + α-Al + Al_4Ca. The fraction of $L1_2$-Al_3Sc/Al_3(Sc,Zr) and $D0_{23}$-Al_3(Sc,Zr) precipitates was calculated and shown in Figure 1e. It was found that as Sc is replaced by Zr, the amount of $L1_2$ phase decreases from 0.251 to 0 at%, while the amount of $D0_{23}$ phase increases from 0 to 0.205 at%.

 doi:10.20944/preprints202512.0932.v1

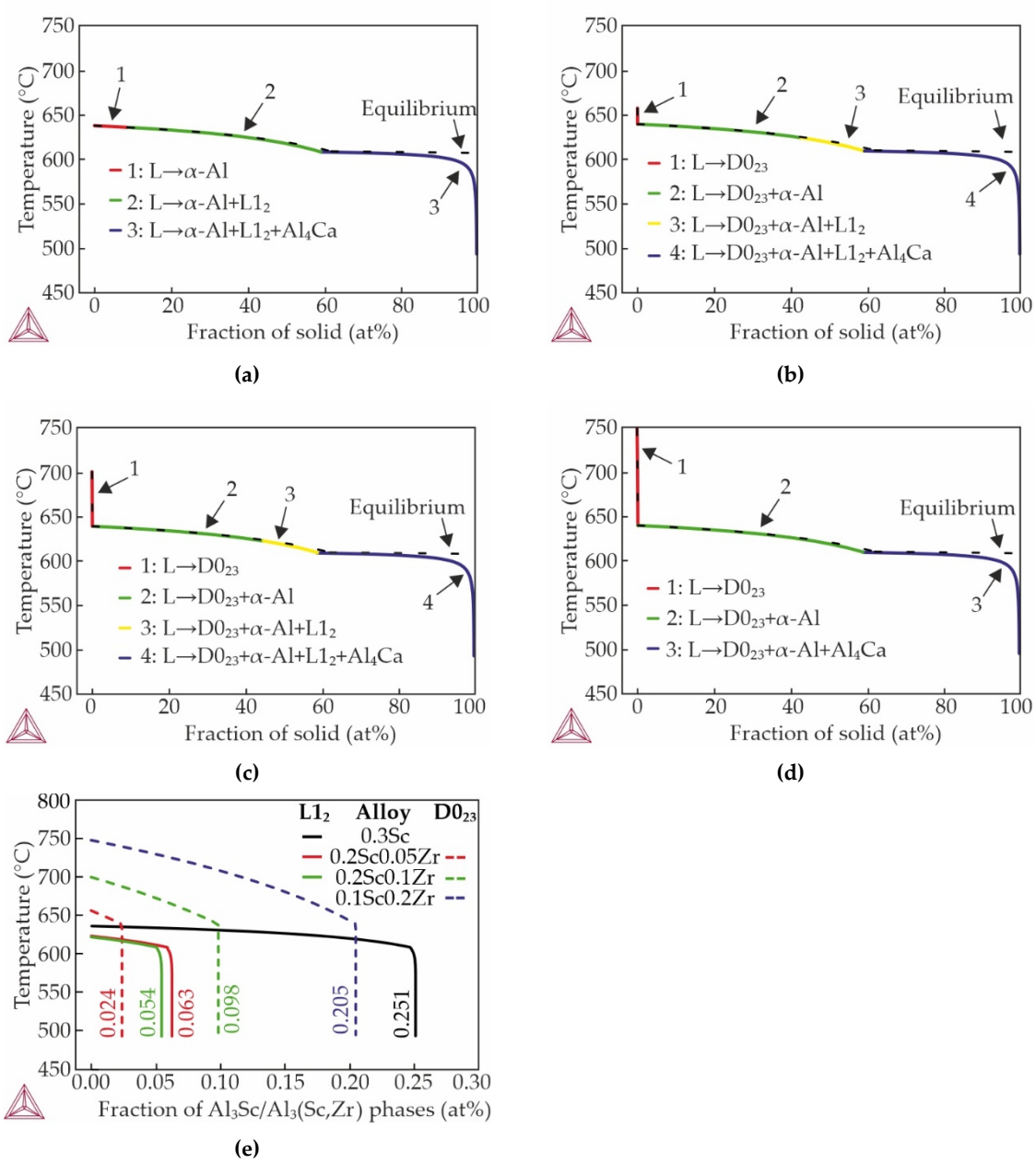

Figure 1. Solidification paths of alloys: (a) AlZn3Ca3Sc0.3, (b) AlZn3Ca3Sc0.2Zr0.05, (c) AlZn3Ca3Sc0.2Zr0.1, (d) AlZn3Ca3Sc0.1Zr0.2 and (e) fraction of $L1_2$–$Al_3Sc/Al_3(Sc,Zr)$ and $D0_{23}$–$Al_3(Sc,Zr)$ phases.

Figure 2 shows the as-cast microstructure of the alloys and the EDS maps showing the alloying elements distribution in the specified region. The structure of the as-cast alloys consists of α-Al dendrites and α-Al+$(Al,Zn)_4Ca$ eutectic, that in partial agreement with calculations in the Thermo-Calc program. Previous studies have indicated that approximately half of Zn contained in the alloys is in the Al_4Ca phase, transforming it into $(Al,Zn)_4Ca$ that cannot be predicted by CALPHAD calculations [15,32]. The calculation of non-equilibrium solidification (Figure 1) indicates the presence of particles of the $L1_2$ and $D0_{23}$ phases in the cast structure of the alloys. However, these phases were not detected in SEM images due to the amount of these precipitates is low.

The low Sc content likely explains the limited precipitation of $L1_2$ and $D0_{23}$ phases, which remain undetectable by EDS analysis. Lohar et al. [33] found that the precipitation of the Al_3Sc and $Al_3(Sc,Zr)$ phases in the structure of as-cast alloys was confirmed only in alloys with a Sc content of 0.5 wt%. Additionally, Shi et al. [34] revealed that the diffraction peaks of the Al_3Sc phase in as-cast alloy were undetected when the total content of Sc and Zr was approximately 0.3 wt%. There is no significant difference in the α-Al+$(Al,Zn)_4Ca$ eutectic structure between the Sc-containing alloy and the Sc,Zr-

 doi:10.20944/preprints202512.0932.v1

containing alloys. The results of the quantitative analysis of the composition of individual particles and structural components of the AlZn3Ca3Sc0.2Zr0.1 alloy are presented in Table 2. The Sc is distributed relatively uniformly in α-Al and in the eutectic region. Conversely, the amount of Zr in the eutectic region is observed to approach zero. This distribution pattern remains consistent across all Zr containing alloys under investigation.

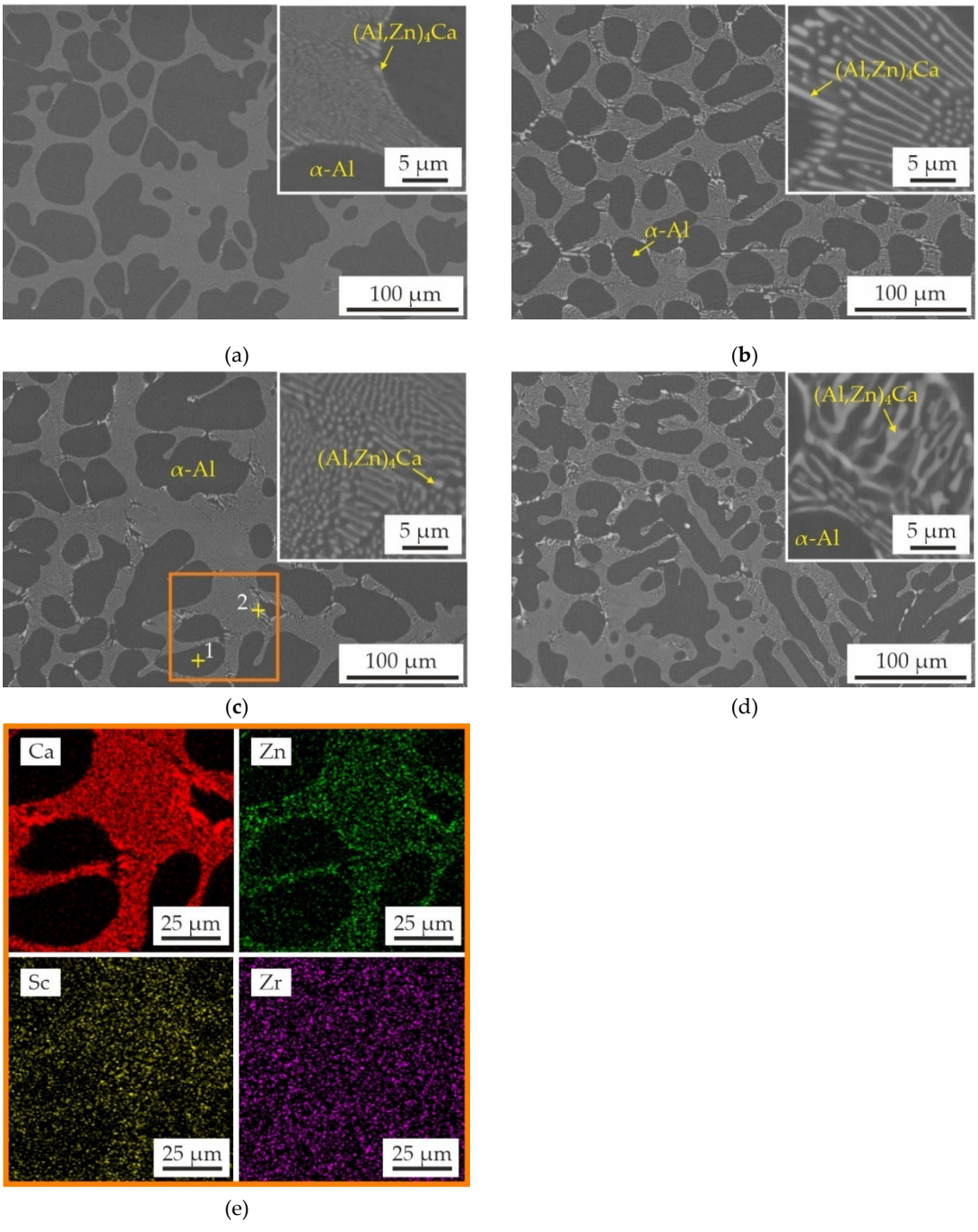

Figure 2. As-cast microstructure (SEM) of (a) AlZn3Ca3Sc0.3, (b) AlZn3Ca3Sc0.2Zr0.05, (c) AlZn3Ca3Sc0.2Zr0.1, (d) AlZn3Ca3Sc0.1Zr0.2 alloys and EDS maps showing alloying elements distribution in selected area (orange rectangle).

Table 2. Composition of structural constituents obtained by EDS in points presented in Figure 2c for AlZn3Ca3Sc0.2Zr0.1.

Points	Element Content (wt%)					Phase/Structure Constituents
	Al	Zn	Ca	Sc	Zr	

 doi:10.20944/preprints202512.0932.v1

1	Bal.	1.11±0.01	0.01±0.01	0.16±0.03	0.30±0.08	α-Al
2	Bal.	10.62±2.40	13.44±3.88	0.13±0.02	0.01±0.01	α-Al+$(Al,Zn)_4Ca$

Figure 3 shows the macrostructure of the as-cast alloys and indicates their average grain sizes. The macrostructure of the alloys consists primarily of relatively large dendritic equiaxed grains. Maximum grain refinement was achieved in the alloy with a Sc/Zr ratio of 0.2/0.05, demonstrating an average grain size of approximately 338 μm, compared to approximately 488 μm for the AlZn3Ca3Sc0.3 alloy. The grain structure of the AlZn3Ca3Sc0.2Zr0.1 and AlZn3Ca3Sc0.1Zr0.2 alloys are virtually similar with the size of 427 and 412 μm, respectively.

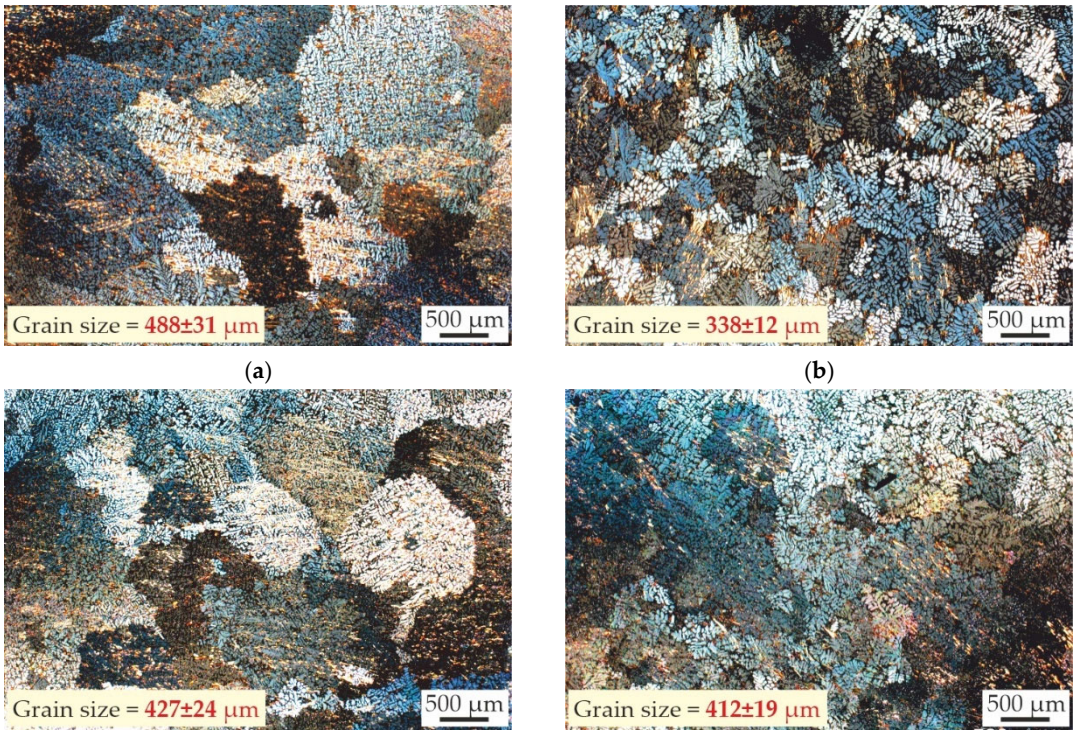

Figure 3. Macrostructure of as-cast alloys: (a) AlZn3Ca3Sc0.3, (b) AlZn3Ca3Sc0.2Zr0.05, (c) AlZn3Ca3Sc0.2Zr0.1, (d) AlZn3Ca3Sc0.1Zr0.2.

The partial replacement of Sc with Zr in all instances results in grain refinement. This suggests that the refining effect resulting from the combined use of Sc and Zr is more pronounced than the effect observed with Sc alone, despite the approximate equivalence in total amount of additives. According to the solidification pathways the Al_3Sc phase in the AlZn3Ca3Sc0.3 alloy precipitates only via the eutectic reaction (Figure 1a). In contrast, in alloys with Zr, solidification begins with the precipitation of primary $Al_3(Sc,Zr)$ particles (Figure 1e). Consequently, the observed grain refinement in Zr-containing alloys can be attributed to the presence of primary $Al_3(Sc,Zr)$ particles that act as effective heterogeneous nucleation sites for aluminum dendrites. Liu et al. [35] noted that heterogeneous nucleation is enhanced in alloys containing Zr and Sc due to the lower interface energy of α-Al/$Al_3(Sc,Zr)$. Similar grain refinement has been documented by other researchers [36,37].

3.2. Effect of Aging Treatment on Hardness and Thermal Conductivity of Alloys

The effect of aging temperature and duration on the hardness of Al–Zn–Ca–Sc–Zr alloys is shown in Figure 4. As can be seen the hardness of the alloys in the as-cast state is almost equal and amounted to 49–52 HB. It is obvious that as the aging temperature increased from 200 to 300 °C, the hardness of the alloys increased, but a further increase in aging temperature resulted in a decrease in hardness. It is worth noting that the effect of aging temperature on hardness is similar for all alloys.

 doi:10.20944/preprints202512.0932.v1

When the aging temperature is 200 °C, the hardness of the alloys increases only slightly during aging and did not exceed 59 HB after 24 h of aging. During aging at 250 °C, the hardness of the alloys increases more intensively and reaches 76–90 HB after 24 h. It has been established that the primary reason for alloys strengthening during aging is the formation of Al_3Sc/Al_3(Sc,Zr) precipitates [38,39]. At temperatures of 300–400 °C, the maximum hardness is attained after 3 h of aging and then remains essentially unaltered for all alloys. With regard to the alloy with 0.3 wt% Sc, it is apparent that at aging temperatures of 350 and 400 °C, subsequent to attaining the peak hardness value, a decrease of hardness is observed. As demonstrated by Watanabe et al., this phenomenon can be attributed to the coarsening and growth of the Al_3Sc particles over the aging time [40]. Concurrently, the Al_3(Sc,Zr) phase is renowned for its thermal stability, which effectively prevents the softening of alloys during prolonged holding periods at high temperatures [41]. The following peak hardness was obtained after aging for 3 h at 300 °C: AlZn3Ca3Sc0.3 – 93 HB, AlZn3Ca3Sc0.2Zr0.5 – 87 HB, AlZn3Ca3Sc0.2Zr0.1 – 83 HB and AlZn3Ca3Sc0.1Zr0.2 – 72 HB. It can be observed that, in general, lower the fraction of Sc in an alloy, the lower the degree of hardening. This tendency is consistent with the results of Lohar et al., which also determined that the hardness increased with increasing Sc content in Al–Sc–Zr alloys after being annealed at 300–470 °C [33].

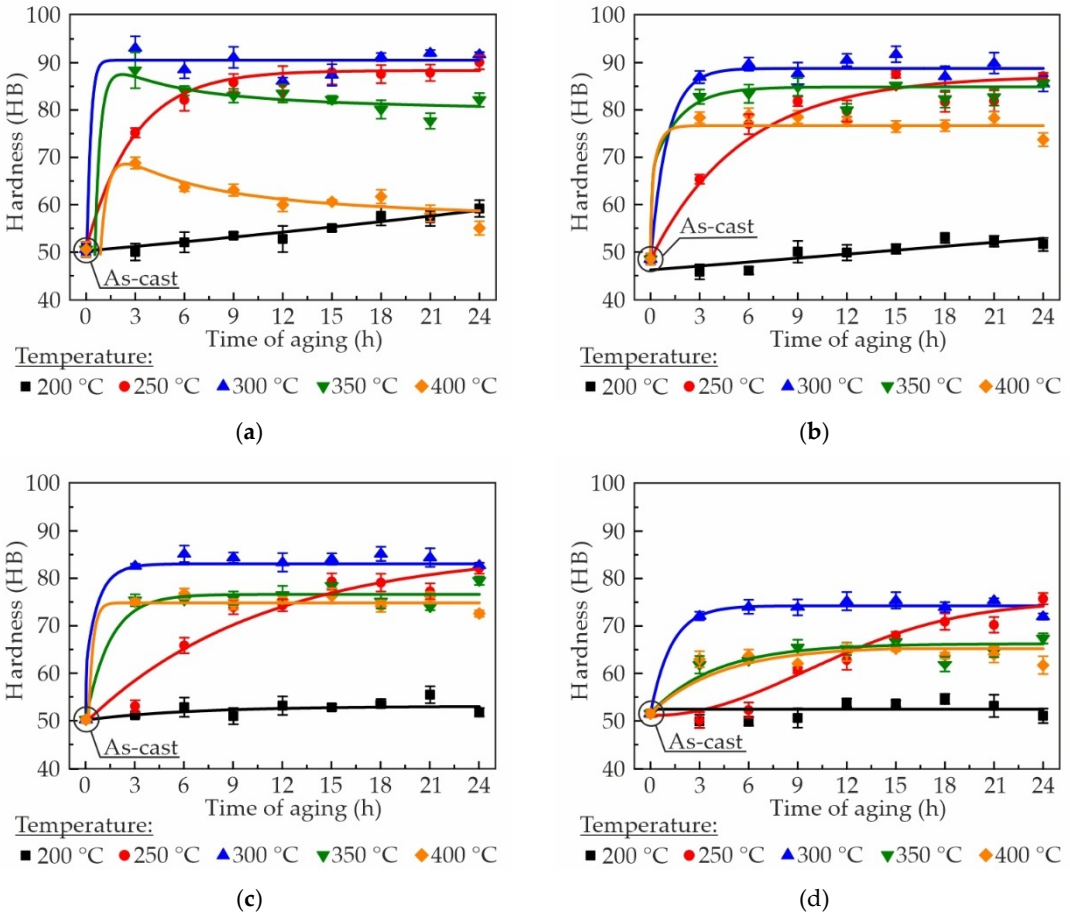

Figure 4. Hardness evolution of the Al–Zn–Ca–Sc–Zr alloys: (a) AlZn3Ca3Sc0.3, (b) AlZn3Ca3Sc0.2Zr0.05, (c) AlZn3Ca3Sc0.2Zr0.1, (d) AlZn3Ca3Sc0.1Zr0.2, during aging treatment at 200–400 °C.

The change in thermal conductivity during the aging treatment at temperatures of 200–400 °C is shown in Figure 5. It was observed that an increase in the fraction of Zr in the as-cast alloys led to a decrease in thermal conductivity from 167.6 to 158.9 W/mK. In metals and alloys, thermal conductivity is primarily determined by the energy transport by free electrons. Thus, any distortion of the lattice, which can be caused by impurities, defects, or dissolved atoms in a solid solution, etc., results in a decrease in thermal conductivity [42,43]. In the present study, the predominant factor

 doi:10.20944/preprints202512.0932.v1

influencing thermal conductivity of alloys in the as-cast condition appears to be lattice strain caused by the saturation of the α-Al solid solution with Zr and/or Sc atoms. As exemplified by the AlZn3Ca3Sc0.2Zr0.1 alloy (Table 2), the distribution of Sc and Zr in the as-cast structure differs, with Zr content in α-Al being approximately twice that of Sc. Consequently, the observed decrease in thermal conductivity is likely due to the increased Zr content in α-Al.

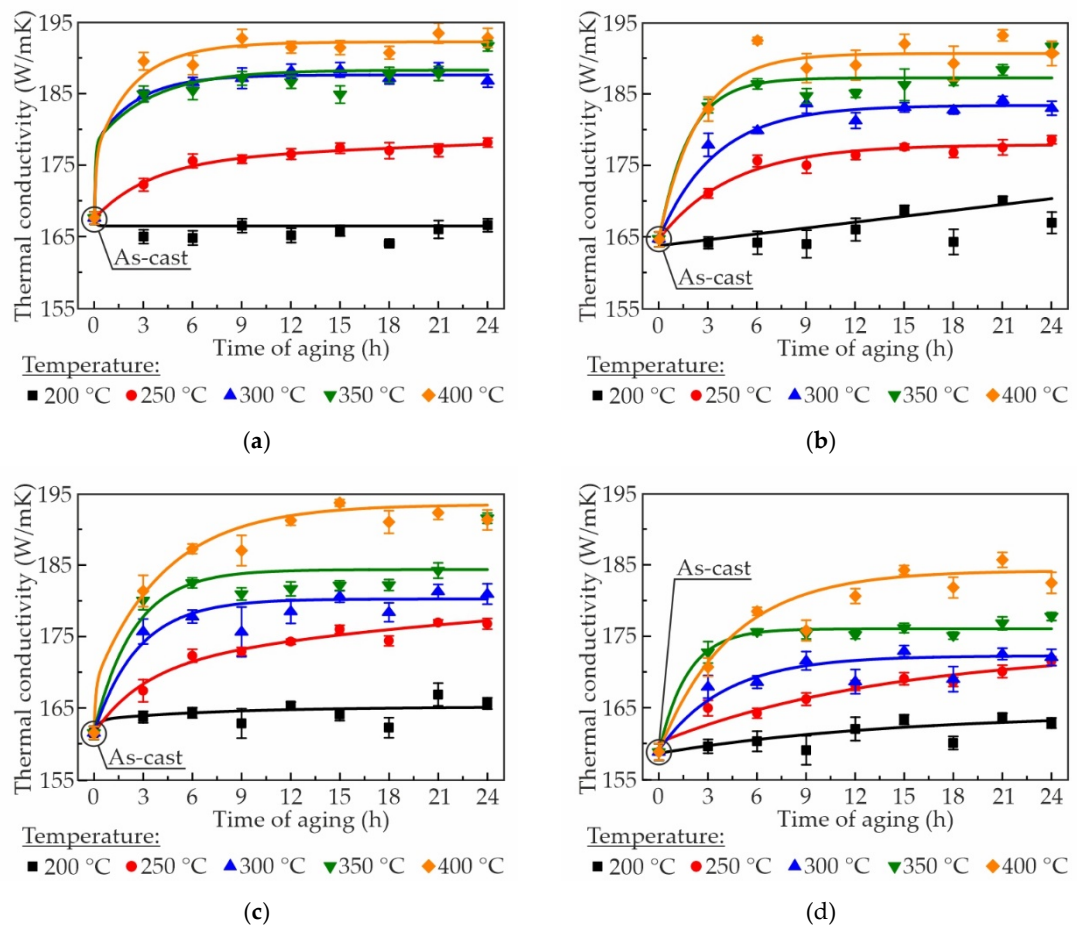

Figure 5. Thermal conductivity evolution of the Al–Zn–Ca–Sc–Zr alloys: (a) AlZn3Ca3Sc0.3, (b) AlZn3Ca3Sc0.2Zr0.05, (c) AlZn3Ca3Sc0.2Zr0.1, (d) AlZn3Ca3Sc0.1Zr0.2, during aging treatment at 200–400 °C.

As illustrated in Figure 5, the thermal conductivity of the alloys exhibited an increase with an elevation in the aging temperature. For example, when the aging time was maintained at 3 hours and the aging temperature increased from 200 to 400 °C, the thermal conductivity of the AlZn3Ca3Sc0.3 alloy exhibited a notable enhancement, rising from 165.0 to 189.5 W/mK. A comparable increase in the Zr-containing alloys was observed. The observed increase in thermal conductivity during aging is likely attributable to the continuous precipitation of $Al_3Sc/Al_3(Sc,Zr)$ phase, which effectively reduces the content of Sc and Zr in α-Al. It has been established that the presence of secondary phases impedes electron mobility to a lesser extent [42,44]. Moreover, the coherence of $Al_3Sc/Al_3(Sc,Zr)$ particles with the matrix further mitigate their impact on electrical resistivity [45]. In consideration of the established correlation between electrical and thermal conductivity of metals as delineated by the Wiedemann-Franz law, it can be deduced that coherent $Al_3Sc/Al_3(Sc,Zr)$ nanoparticles should not substantially decrease the thermal conductivity of alloys. With regard to the aging time, the outcome was analogous to that observed for hardness: the majority of alloys reached their peak thermal conductivity within a period of 3–6 hours. Following this initial peak, subsequent aging had a negligible effect on hardness. In summary, it was evident that the mechanical properties and thermal conductivity of Al–Zn–Ca–Sc–Zr alloys could be optimized through the change of aging parameters.

 doi:10.20944/preprints202512.0932.v1

The most promising heat treatment regime was aging during 3 hours at 300 °C, as this regime was found to simultaneously achieve the highest hardness and moderate thermal conductivity.

3.3. Mechanical Properties and TEM Analysis of as-Aged Alloys

Figure 6 shows the stress-strain curves of the Al–Zn–Ca–Sc–Zr alloys after 3 h aging at 300 °C. The mechanical properties of the alloys are presented in Table 3. Although the AlZn3Ca3Sc0.3 alloy possesses a larger average grain size (Figure 3a), it demonstrated superior mechanical properties compared to alloys comprising Zr. The substitution of Sc with Zr led to a decrease in tensile yield strength (TYS) from 217.5 to 137.2 MPa and ultimate tensile strength (UTS) from 269.0 to 206.3 MPa, while elongation at fracture (El) increased from 4.6 to 7.1%. It is evident that the alteration in grain size does not serve as a pivotal factor influencing strengthening. The observed strength reduction with increasing Zr content correlates with decreased Sc concentration in the alloys. These findings are consistent with those reported by Yang J. et al. [46], who found that Zr additions exceeding 0.1 wt% in Al–6.5Mg–0.50Mn–0.25Sc–Zr alloys leads to formation of coarse primary Al_3(Sc,Zr) particles at higher Zr concentrations, which diminishes the effectiveness of precipitation strengthening. As illustrated in Figure 1e, the proportion of primary $D0_{23}$-Al_3(Sc,Zr) crystals in the studied alloys increases, while the proportion of phase $L1_2$-Al_3(Sc,Zr) decreases. This, in turn, could also lead to a decrease in the efficiency of precipitation strengthening.

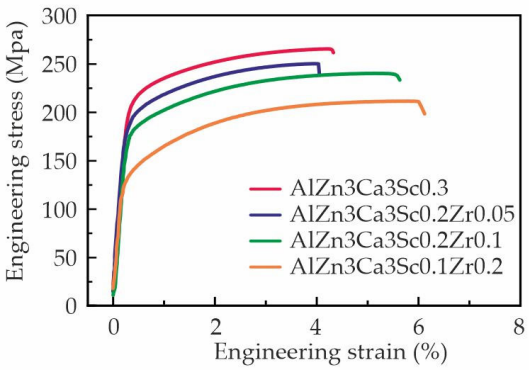

Figure 6. The engineering stress-strain curves of the aged during 3h at 300 °C Al–Zn–Ca–Sc–Zr alloys.

Table 3. Mechanical properties of the Al–Zn–Ca–Sc–Zr alloys with different Sc/Zr ratios after aging at 300 °C for 3h.

Specimen designation		TYS (MPa)	UTS (MPa)	El (%)
#1	AlZn3Ca3Sc0.3	217.5±5.8	269.0±6.9	4.6±1.0
#2	AlZn3Ca3Sc0.2Zr0.05	195.2±1.5	250.7±2.0	4.5±1.0
#3	AlZn3Ca3Sc0.2Zr0.1	180.9±4.8	235.3±6.6	5.1±2.2
#4	AlZn3Ca3Sc0.1Zr0.2	137.2±5.4	206.3±6.1	7.1±2.0

Figure 7 shows TEM images of the AlZn3Ca3Sc0.3 and AlZn3Ca3Sc0.2Zr0.1 alloys that were aged at 300 °C for 3 h. The images in Figure 7a–c were obtained along the $[01\bar{1}]_{Al}$ zone axis, while those in Figure 7d–f were obtained along the $[001]_{Al}$ zone axis. The diffraction patterns revealed that the precipitated phases correspond to an $L1_2$-ordered structure. The $L1_2$-Al_3Sc and $L1_2$-Al_3(Sc,Zr) precipitates have a nearly spherical shape, and the precipitates exhibit a "coffee bean" contrast (Figure 7a), indicating their coherence with the Al matrix. The obtained images provide evidence that the high hardness and strength of the alloys are attributable to the strengthening resulting from the precipitation of phases with $L1_2$ structure.

 doi:10.20944/preprints202512.0932.v1

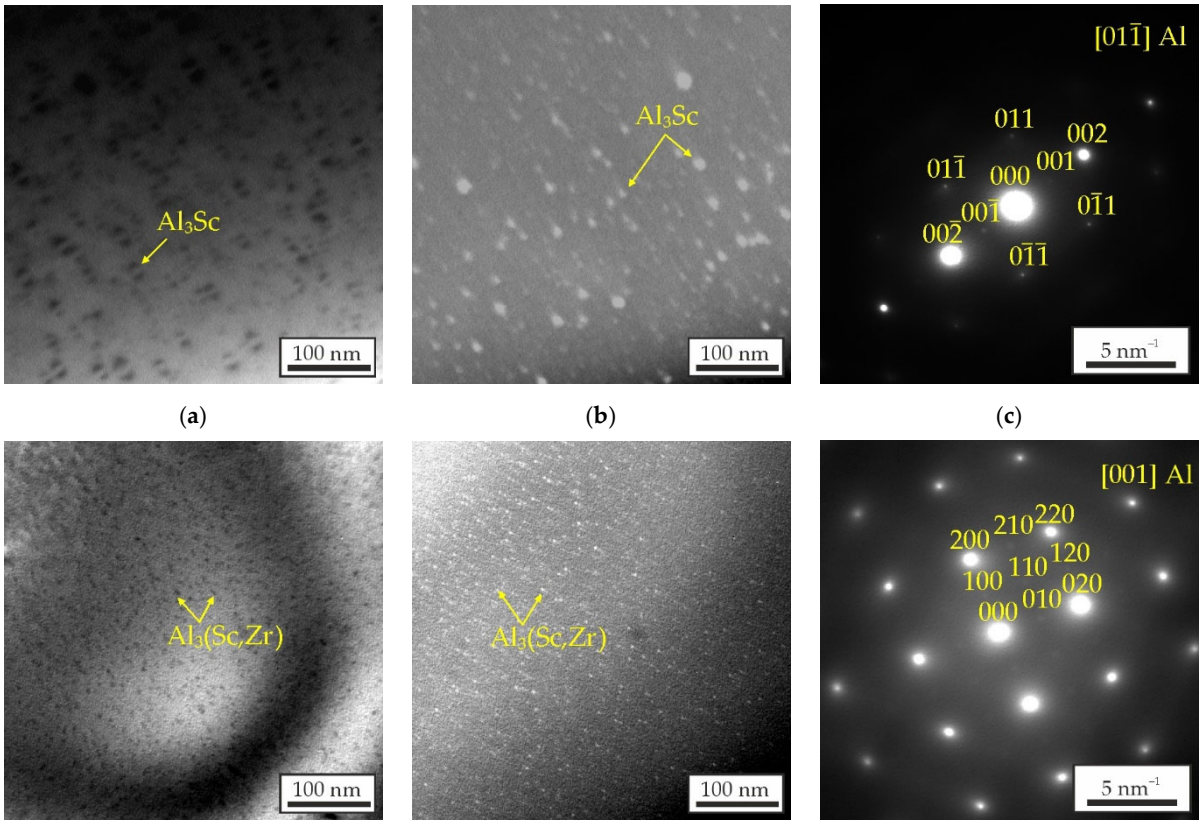

Figure 7. TEM (a), (d) bright field images, (b), (c) dark field image and (c), (f) selected area diffraction patterns of aged for 3 h at 300 °C (a), (b), (c) AlZn3Ca3Sc0.3 and (d), (e), (f) AlZn3Ca3Sc0.2Zr0.1 alloys.

Figure 8 shows the effect of aging time and temperature on the precipitate diameter according to the calculation results in Thermo-Calc for the Al-Zr-Sc alloys (AlSc0.3 and AlSc0.2Zr0.1). The Ca and Zn was excluded from the calculation due to the calculation errors connected with shortcoming of used software. The calculation indicates that the diameter of $L1_2$-Al_3Sc/$L1_2$-$Al_3(Sc,Zr)$ precipitates should increase with increasing aging temperature and holding time. According to calculations performed, the $L1_2$-Al_3Sc/$L1_2$-$Al_3(Sc,Zr)$ precipitates after aging at 300 °C for 3 hours should have a diameter of approximately 14 nm for both AlSc0.3 and AlSc0.2Zr0.1 alloys. However, the experimentally determined average precipitate diameter was found to be considerably smaller. The average diameter determined by TEM images of $L1_2$-Al_3Sc/$L1_2$-$Al_3(Sc,Zr)$ precipitates in the AlZn3Ca3Sc0.3 and AlZn3Ca3Sc0.2Zr0.1 alloys aged at 300 °C for 3 hours was 8.56 ± 0.39 and 2.39 ± 0.04 nm, respectively. Furthermore, it is evident that the substitution of Sc with Zr resulted in a decrease of the precipitate diameter. Fuller et al. [47] investigated the evolution of the size of precipitates $Al_3(Sc_{1-x}Zr_x)$ as a function of aging time at 300 °C and found that $Al_3(Sc,Zr)$ precipitates have greater resistance to coarsening than Al_3Sc.

 doi:10.20944/preprints202512.0932.v1

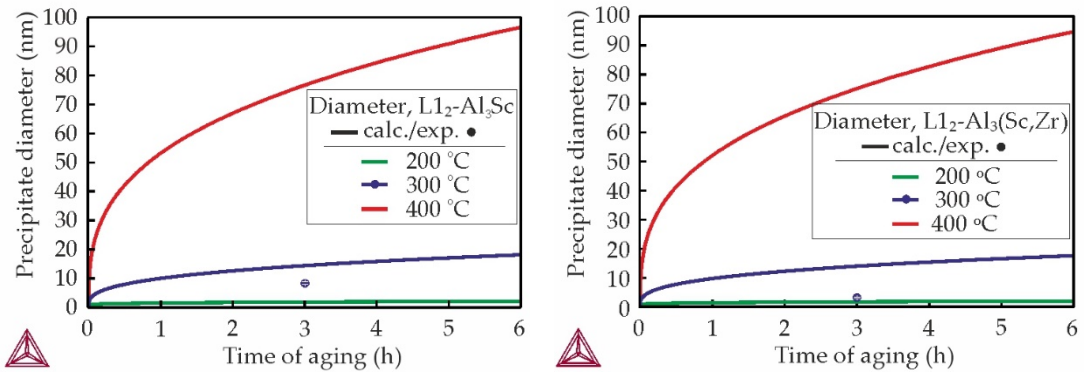

Figure 8. Calculated diameter of $Al_3Sc/Al_3(Sc,Zr)$ precipitates in Al-Sc-Zr alloys after aging at 200-400 °C (solid lines): (a) Al–0.3wt%Sc and (b) Al–0.2wt%Sc–0.1wt%Zr. Experimental average diameter of precipitates in (a) AlZn3Ca3Sc0.3 and (b) AlZn3Ca3Sc0.2Zr0.1 alloy following 3 h aging at 300 °C, as determined by TEM (dots).

3.4. Effect of Sc and Zr on Corrosion Properties of as-Aged Alloys

Figure 9 presents the corrosion rates of as-aged Al–Zn–Ca–Sc–Zr alloys determined by immersion corrosion testing. The corrosion rate of the alloy with 0.3 wt% Sc was approximately 0.022 mm/year, while partial substitution of Sc with Zr reduced corrosion rates to 0.002–0.006 mm/year. According the graph, variations in Zr content within 0.05–0.2 wt% did not substantially affect corrosion rates, indicating that even minimal Zr additions (0.05 wt%) effectively enhance corrosion resistance.

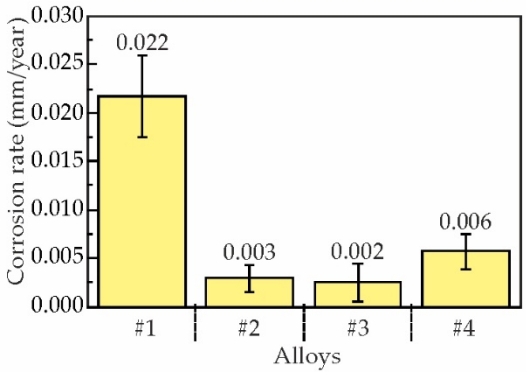

Figure 9. Corrosion rate of the as-aged Al–Zn–Ca–Sc–Zr alloys (300 °C, 3 h) determined after 15 day immersion test in 5.7% NaCl + 0.3% H_2O_2 solution: #1 – AlZn3Ca3Sc0.3, #2 – AlZn3Ca3Sc0.2Zr0.05, #3 – AlZn3Ca3Sc0.2Zr0.1, #4 – AlZn3Ca3Sc0.1Zr0.2.

Cross-sections of the samples after immersion corrosion testing revealed that the majority of the surfaces exhibited minimal alterations, with instances of corrosion cavity being infrequent. The cross-sections images of the as-aged alloys specimens with typical corrosion cavities and the average corrosion cavity depth (ACC) after immersion corrosion testing are presented in Figure 10. It is evident that local corrosion damage developed from the outer to the inner regions of the alloy along the eutectic area in alloy structure. As previously established in [48], Al–Ca–Si alloys exhibit enhanced corrosion resistance, attributable to their refined eutectic structures, which impede the penetration of corrosion cavity depth into the alloy. In the present study, the eutectic lamellas of the $(Al,Zn)_4Ca$ phase, acting as an anode, likely played a pivotal role in the high corrosion resistance of the alloys. According to the findings reported in [49–51], Al_3Sc and $Al_3(Sc,Zr)$ particles function as cathodes in relation to the Al matrix, thereby facilitating the progression of pitting corrosion. However, Cavanaugh et al. [49] found that the kinetics of the cathodic reaction of Al_3Sc/Al is sluggish

 doi:10.20944/preprints202512.0932.v1

and should not pose a major corrosion risk. The AlZn3Ca3Sc0.3 alloy exhibited the average corrosion depth cavity of 27.8±8.0 μm. In comparison, the alloy with 0.2 wt% Zr demonstrated average corrosion cavity depth of 10.1±1.1 μm. The observed discrepancy in the corrosion cavity depth indicates that increasing the ratio of Zr can enhance the corrosion resistance of the Al–Zn–Ca–Sc–Zr alloys to local corrosion. Furthermore, when alloying with 0.05 wt% Zr (Figure 10b), although substantial corrosion cavities remain, yet their prevalence on the specimen's surface has diminished, as substantiated by the diminished corrosion rate of the alloy (Figure 9).

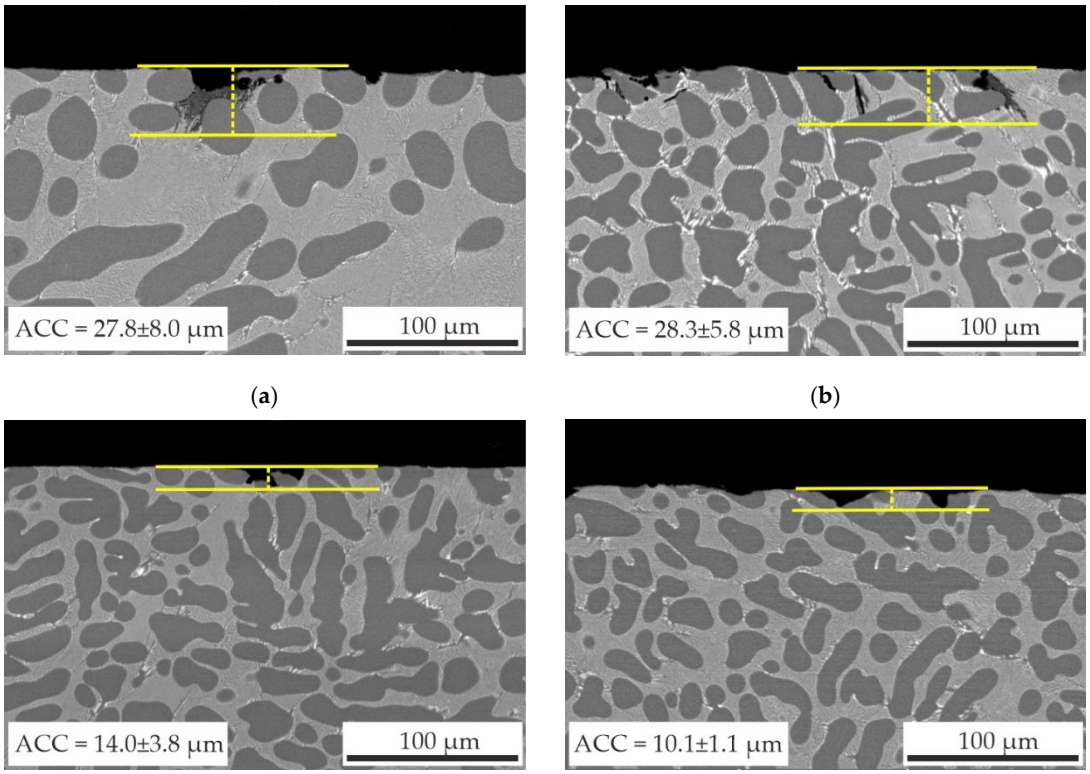

Figure 10. Cross-sectional microstructure and average corrosion cavity depths (ACD) of as-aged specimens of alloys: (a) AlZn3Ca3Sc0.3, (b) AlZn3Ca3Sc0.2Zr0.05, (c) AlZn3Ca3Sc0.2Zr0.1 and (d) AlZn3Ca3Sc0.1Zr0.2 after 15 day immersion test in 5.7% NaCl + 0.3% H_2O_2 solution.

Typical polarization curves obtained for as-aged Al–Zn–Ca–Sc–Zr alloys in a solution of 5.7% NaCl + 0.3% H_2O_2 with distilled water are shown in Figure 11. The corrosion characteristics of the alloys, including open circuit potential (OCP) and the corrosion potentials (E_{corr}), were obtained. The OCP evolution was monitored over time for all specimens prior to electrochemical testing, with results presented in Figure 11a. The OCP values were found to stabilize at approximately −950 mV for all alloys, indicating that the corrosion resistance characteristics of the investigated compositions were approximately similar. Figure 11b shows the potentiodynamic polarization curves. For all alloys, the cathodic branch of the polarization curve manifests conventional characteristics of diffusion control within a non-mixing electrolyte. The anode branch of the polarization curve for all alloys displays a passive region, accompanied by a subsequent transition to pitting at a breakdown potential (E_b) of approximately –900 mV. Additionally, it has been observed that alloys with a higher amount of Zr exhibit more positive E_b, indicating that increasing the ratio of Zr contributes to enhancing the stability of the passive film on the surface of the specimens. The E_{corr} of the alloys ranges from –1.17 to –1.21 V, and the addition of Zr can shift the E_{corr} slightly to the more negative values. A faster transition to the anodic region and broader passive region of Zr containing alloys in comparison to alloy without Zr (AlZn3Ca3Sc0.3) indicates faster passivation, which leads to better

 doi:10.20944/preprints202512.0932.v1

corrosion resistance in this electrolyte. The distinction between OCP and E_{corr} is attributable to the passive film that is formed in this electrolyte.

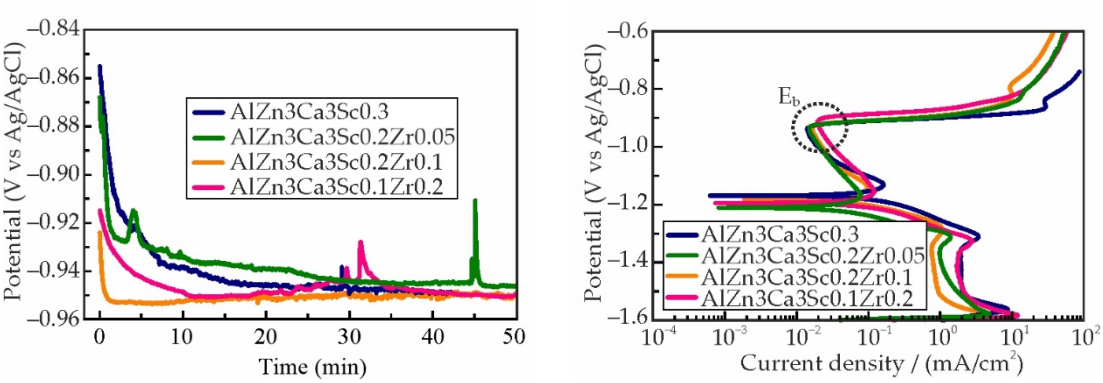

(**a**) (**b**)

Figure 11. (a) Evolution of the OCP versus exposure time and (b) Polarisation curves of as-aged Al–Zn–Ca–Sc–Zr alloys in 5.7% NaCl + 0.3% H_2O_2 solutions.

Thus, the corrosion tests demonstrated that addition of Zr has positive effect on the corrosion resistance of Al–Zn–Ca–Sc–Zr alloys. Kozlova et al. [52] also discovered that $Al_3(Sc,Zr)$ particles with a substantial Zr proportion exert a less pronounced effect on the corrosion rate in comparison to Al_3Sc. The authors attribute this phenomenon to a decrease in the number of $Al_3(Sc,Zr)$ particles caused by a decrease in the total content of Sc and Zr (at%) when replacing Sc with Zr due to the difference in atomic mass between these two elements. At the same time in this work, it was established that the $L1_2$-Al_3Sc/$L1_2$-$Al_3(Sc,Zr)$ precipitates in AlZn3Ca3Sc0.2Zr0.1 alloy is more than 3 times finer than in AlZn3Ca3Sc0.3 aloy (Figure 7 and 8) and that also can be a reason of the higher corrosion resistance of alloys with Zr addition.

3.5. Thermal Conductivity of Al–3wt%Zn–3wt%Ca–0.3wt%Sc Alloy

The alloy exhibiting the highest thermal conductivity in accordance with Equation (1) was selected for the additional thermal conductivity investigations using Equation (2). The thermal properties and density of the AlZn3Ca3Sc0.3 alloy after aging are shown in Figure 12. As the temperature rises, thermal diffusivity undergoes a progressive decrease, and conversely, heat capacity experiences an increase. Concurrently, a slight decrease in the density is exhibited, attributable to thermal expansion. The interplay between these parameters leads to a negligible variation in thermal conductivity calculated in accordance with Equation (2) across the studied temperature range. As the temperature increases from room temperature to 132 °C, the thermal conductivity of the alloys exhibits a slight increase, from 159.6 to 161.4 W/mK. A further increase in temperature to 300 °C results in a slight decrease in thermal conductivity, which reaches 159.0 W/mK. These changes remain within the 1% range, suggesting that thermal conductivity remains essentially constant across this temperature range. Furthermore, the calculated thermal conductivity is 14% lower than that obtained using Equation (1), that was 184.7 W/mK. The thermal conductivity of pure aluminum at room temperature is 235 W/mK [53], and the thermal conductivity of the AlZn3Ca3Sc0.3 alloy is approximately 68% of the pure aluminum thermal conductivity.

 doi:10.20944/preprints202512.0932.v1

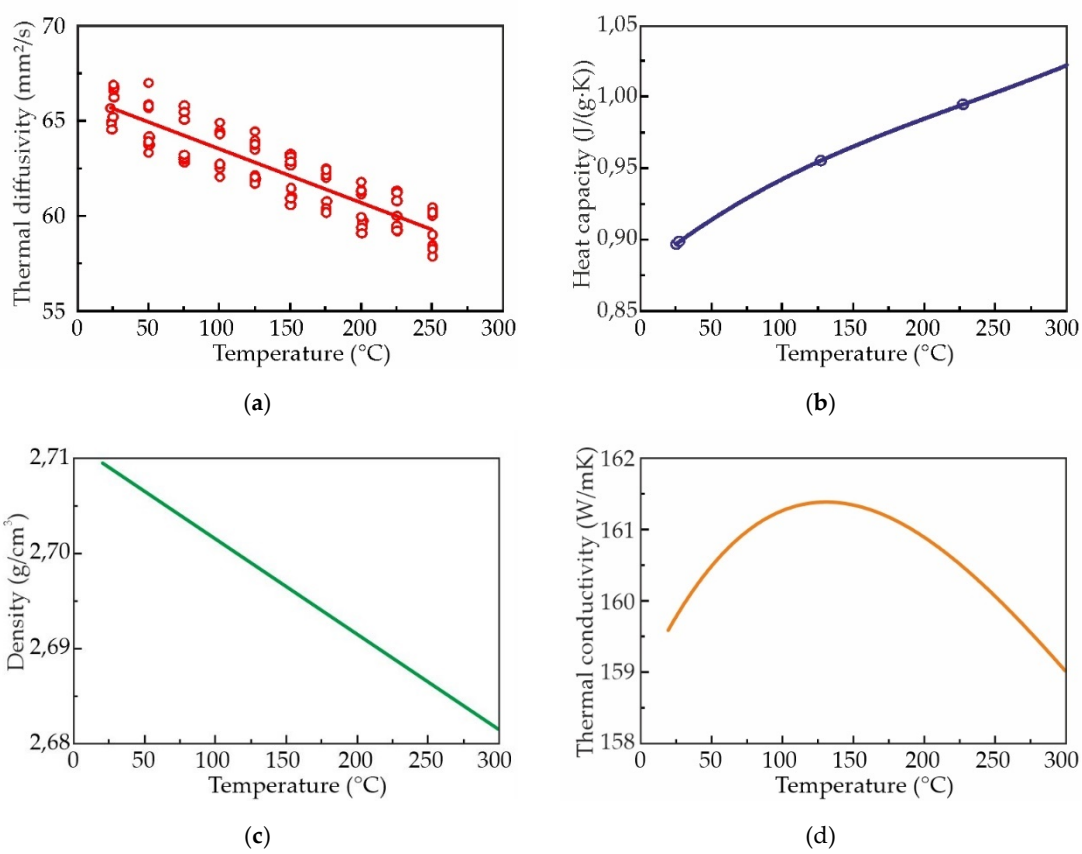

Figure 12. (a) Thermal diffusivity, (b) heat capacity, (c) density and (d) thermal conductivity of the as-aged AlZn3Ca3Sc0.3 alloy.

4. Conclusions

In this study, the effect of Sc and Zr (total content: 0.3 wt.%) on the Al–3 wt% Zn–3 wt% Ca alloy properties were investigated. The following conclusions can be drawn from the present investigation:

1. The microstructure of the as-cast alloys consists of α-Al dendrites and refined lamellas of α-Al+$(Al,Zn)_4Ca$ eutectic. Sc was found to be uniformly distributed throughout the aluminum matrix, while Zr was concentrated in the center of dendritic cells. All alloys demonstrated coarse grain structure, but the addition of Zr lead to a little decrease of the grain size. The minimal grain size of 338 μm was observed for alloy with 0.2 wt% Sc and 0.05 wt% Zr.
2. In the as-cast state, the substitution of scandium with zirconium did not result in a substantial alteration of the alloys' hardness, and is was approximately 50 HB. However, this substitution did lead to a decline in the thermal conductivity of the alloys, with a decrease from 167.6 to 158.9 W/mK (calculated via Smith-Palmer equation).
3. The most suitable heat treatment regime was determined to be the aging treatment at 300 °C for 3 h. This regime resulted in a substantial enhancement of the alloys hardness to 93 HB and thermal conductivity obtained, via the Smith and Palmer equation, to ~185 W/mK. However, increasing of the Zr content led to a decrease in hardness and thermal conductivity in as-aged alloys.
4. The Al–Zn–Ca–Sc–Zr alloys exhibit high mechanical properties in as-aged state due to the precipitation of strengthening $Al_3Sc/Al_3(Sc,Zr)$ phase during the aging process. However, substituting Sc with Zr results in a decrease in the UTS of the alloys from 269 to 206 MPa and an increase in their El from 4.6 to 7.1%. The highest strength was obtained in the alloy with 0.3% Sc.
5. The immersion corrosion test results demonstrated that replacing Sc with Zr can reduce the corrosion rate of as-aged alloys from 0.022 to 0.002–0.006 mm/year and reduce the average corrosion cavity depth from 27.8±8.0 μm to 10.1±1.1 μm. Electrochemical corrosion testing has

 doi:10.20944/preprints202512.0932.v1

demonstrated that the partial substitution of Sc with Zr in alloy compositions enhances the resistance of the alloys to pitting corrosion.

6. The thermal conductivity of the AlZn3Ca3Sc0.3 alloy in as-aged condition, that was determined using the thermal diffusivity equation, to be approximately 160 W/mK at room temperature. This value is equivalent to 68% of the thermal conductivity exhibited by pure aluminum.

Author Contributions: Conceptualization, A.L.; methodology, V.B.; software, V.B.; validation, A.K.; formal analysis, V.B.; investigation, I.B., M.G., O.V., A.S., V.D., R.B. and Sh.R.; resources, A.L.; data curation, V.B.; writing—original draft preparation, A.L.; writing—review and editing, A.L. and V.B.; visualization, A.L.; supervision, V.B.; project administration, V.B.; funding acquisition, V.B. All authors have read and agreed to the published version of the manuscript.

Funding: This research was funded by the Russian Science Foundation, Project Number 24-29-00682.

Institutional Review Board Statement: Not applicable.

Informed Consent Statement: Not applicable.

Data Availability Statement: The original contributions presented in this study are included in the article. Further inquiries can be directed to the corresponding author.

Conflicts of Interest: The authors declare no conflict of interest.

References

1. Smith, L.J.B.; Corbin, S.F.; Hexemer Jr., R.L.; Donaldson, I.W.; Bishop, D.P. Development and Processing of Novel Aluminum Powder Metallurgy Materials for Heat Sink Applications. *Metall. Mater. Trans. A* **2013**, *45*, 980-989. https://doi.org/10.1007/s11661-013-2011-5
2. Haga, T.; Fuse, H. Die Casting of Lightweight Thin Fin Heat Sink Using Al-25%Si. *Metals* **2024**, *14*, 622. https://doi.org/10.3390/met14060622
3. Jou, R.Y. Convective Heat Transfer Measurements of Die-Casting Heat Sinks. *Key Eng. Mater.* **2010**, *419*, 345-348. https://doi.org/10.4028/www.scientific.net/KEM.419-420.345
4. Sce, A.; Caporale, L. High Density Die Casting (HDDC): New Frontiers in the Manufacturing of Heat Sinks. *J. Phys. Conf. Ser.* **2014**, *525*, 012020. https://doi.org/10.1088/1742-6596/525/1/012020
5. Gan, J.; Huang, Y.; Wen, C.; Du, J. Effect of Sr Modification on Microstructure and Thermal Conductivity of Hypoeutectic Al–Si Alloys. *Trans. Nonferrous Met. Soc. China* **2020**, *30*, 2879-2890. https://doi.org/10.1016/S1003-6326(20)65428-0
6. Cho, Y.H.; Kim, H.W.; Lee, J.M.; Kim, M.S. A New Approach to the Design of a Low Si-Added Al–Si Casting Alloy for Optimising Thermal Conductivity and Fluidity. *J. Mater. Sci.* **2015**, *50*, 7271-7281. https://doi.org/10.1007/s10853-015-9282-8
7. Zhang, W.; Hu, S.; Wang, K.; Huang, Y.; Zhong, Y.; Li, W. Effect of Silicon Micro-Alloying on the Thermal Conductivity, Mechanical Properties and Rheological Properties of the Al–5Ni Cast. *Int. J. Metalcast.* **2024**, *18*, 3277-3291. https://doi.org/10.1007/s40962-023-01255-8
8. Lou, G.; Zhou, X.; Li, C.; Du, J. Design and Preparation of Al-Fe-Ce Ternary Aluminum Alloys with High Thermal Conductivity. *Trans. Nonferrous Met. Soc. China* **2022**, *32*, 1781-1794. https://doi.org/10.1016/S1003-6326(22)65908-9
9. Kotiadis, S.; Zimmer, A.; Elsayed, A.; Vandersluis, E.; Ravindran, C. High Electrical and Thermal Conductivity Cast Al-Fe-Mg-Si Alloys with Ni Additions. *Metall. Mater. Trans. A* **2020**, *51*, 4195-4214. https://doi.org/10.1007/s11661-020-05826-w
10. Bazhenov, V.E.; Koltygin, A.V.; Sung, M.C.; Park, S.H.; Tselovalnik, Y.V.; Stepashkin, A.A.; Rizhsky, A.A.; Belov, M.V.; Belov, V.D.; Malyutin, K.V. Development of Mg–Zn–Y–Zr Casting Magnesium Alloy with High Thermal Conductivity. *J. Magnes. Alloys* **2021**, *9*, 1567-1577. https://doi.org/10.1016/j.jma.2020.11.020
11. Belov, N.A.; Naumova, E.A.; Bazlova, T.A.; Alekseeva, E.V. Structure, Phase Composition, and Strengthening of Cast Al–Ca–Mg–Sc Alloys. *Phys. Met. Metallogr.* **2016**, *117*, 188-194. https://doi.org/10.1134/S0031918X16020046

 doi:10.20944/preprints202512.0932.v1

12. Naumova, E.A. Use of Calcium in Alloys: From Modifying to Alloying. *Russ. J. Non-Ferrous Met.* **2018**, *59*, 284-298. https://doi.org/10.3103/S1067821218030100
13. Letyagin, N.V.; Musin, A.F.; Sichev, L.S. New Aluminum-Calcium Casting Alloys Based on Secondary Raw Materials. *Mater. Today Proc*. **2021**, *38*, 1551-1555. https://doi.org/10.1016/j.matpr.2020.08.148
14. Kevorkov, D.; Schmid-Fetzer, R. The Al-Ca System, Part 1: Experimental Investigation of Phase Equilibria and Crystal Structures. *Int. J. Mater. Res*. **2001**, *92*, 946-952. https://doi.org/10.1515/ijmr-2001-0172
15. Lyskovich, A.A.; Bazhenov, V.E.; Komissarov, A.A.; Koltygin, A.V.; Belov, V.D. Development of Al-Zn-Ca Casting Aluminum Alloy with High Thermal Conductivity for Electronics and Electric Vehicle Industry. In *Non-Ferrous Metals and Minerals - 2024: Book of Abstracts of the Twelfth International Congress, Krasnoyarsk, Russia, 9–13 September* 2024; p. 504.
16. Lv, Q.; Zhang, F.; Wei, H.; Li, Z.; Zhang, J. Effect of Rare Earth (La, Ce, Nd, Sc) on Strength and Toughness of 6082 Aluminum Alloy. *Vacuum* **2023**, *215*, 112333. https://doi.org/10.1016/j.vacuum.2023.112333
17. Wan, W.; Han, J.; Li, W.; Wang, J. Study of Rare Earth Element Effect on Microstructures and Mechanical Properties of an Al-Cu-Mg-Si Cast Alloy. *Rare Met.* **2006**, *25*, 129-132. https://doi.org/10.1016/S1001-0521(08)60066-2
18. Zakharov, V.V. Effect of Scandium on the Structure and Properties of Aluminum Alloys. *Met. Sci. Heat Treat.* **2003**, *45*, 246-253. https://doi.org/10.1023/A:1027368032062
19. Zhou, S.A.; Zhang, Z.; Li, M.; Pan, D.; Su, H.; Du, X.; Li, P.; Wu, Y. Effect of Sc on Microstructure and Mechanical Properties of As-Cast Al–Mg Alloys. *Mater. Des.* **2016**, *90*, 1077-1084. https://doi.org/10.1016/j.matdes.2015.10.132
20. Costa, S.; Puga, H.; Barbosa, J.; Pinto, A.M.P. The Effect of Sc Additions on the Microstructure and Age Hardening Behaviour of As Cast Al–Sc Alloys. *Mater. Des*. **2012**, *42*, 347-352. https://doi.org/10.1016/j.matdes.2012.06.019
21. Norman, A.F.; Prangnell, P.B.; McEwen, R.S. The Solidification Behaviour of Dilute Aluminium–Scandium Alloys. *Acta Mater*. **1998**, *46*, 5715-5732. https://doi.org/10.1016/S1359-6454(98)00257-2
22. Xu, C.; Xiao, W.; Zheng, R.; Hanada, S.; Yamagata, H.; Ma, C. The Synergic Effects of Sc and Zr on the Microstructure and Mechanical Properties of Al–Si–Mg Alloy. *Mater. Des.* **2015**, *88*, 485-492. https://doi.org/10.1016/j.matdes.2015.09.045
23. Forbord, B.; Lefebvre, W.; Danoix, F.; Hallem, H.; Marthinsen, K. Three Dimensional Atom Probe Investigation on the Formation of Al_3(Sc,Zr)-Dispersoids in Aluminium Alloys. *Scr. Mater*. **2004**, *51*, 333-337. https://doi.org/10.1016/j.scriptamat.2004.03.033
24. Deng, P.; Mo, W.; Ouyang, Z.; Tang, C.; Luo, B.; Bai, Z. Mechanical Properties and Corrosion Behaviors of (Sc, Zr) Modified Al-Cu-Mg Alloy. *Mater. Charact*. **2023**, *196*, 112619. https://doi.org/10.1016/j.matchar.2022.112619
25. Scheil, E. Bemerkungen zur Schichtkristallbildung. *Int. J. Mater. Res*. **1942**, *34*, 70-72. https://doi.org/10.1515/ijmr-1942-340303
26. Andersson, J.O.; Helander, T.; Höglund, L.; Shi, P.; Sundman, B. Thermo-Calc & DICTRA, Computational Tools for Materials Science. *Calphad* **2002**, *26*, 273-312. https://doi.org/10.1016/S0364-5916(02)00037-8
27. Klemens, P.G.; Williams, R.K. Thermal Conductivity of Metals and Alloys. *Int. Met. Rev*. **1986**, *31*, 197-215. https://doi.org/10.1179/imtr.1986.31.1.197
28. Poirier, D. R.; Mcbride, E. A Thermal conductivities of hypoeutectic AI-Cu alloys during solidification and cooling. *Mater. Sci. Eng. A* **1997**, *224*, 48-52.
29. Chase, M.W. NIST-JANAF Thermochemical Tables. *J. Phys. Chem. Ref. Data* **1998**, *28*, 1951-1951.
30. *ASTM G110-92*; Standard Practice for Evaluating Intergranular Corrosion Resistance of Heat Treatable Aluminum Alloys by Immersion in Sodium Chloride + Hydrogen Peroxide Solution; ASTM International: West Conshohocken, PA, USA, 2003.
31. *ASTM G1-03*; Standard Practice for Preparing, Cleaning, and Evaluating Corrosion Test Specimens; ASTM International: West Conshohocken, PA, USA, 2011.
32. Belov, N.A.; Naumova, E.A.; Akopyan, T.K. Effect of Calcium on Structure, Phase Composition and Hardening of Al-Zn-Mg Alloys Containing up to 12 wt.% Zn. *Mater. Res*. **2015**, *18*, 1384-1391. http://dx.doi.org/10.1590/1516-1439.036415

 doi:10.20944/preprints202512.0932.v1

33. Lohar, A.K.; Mondal, B.; Rafaja, D.; Klemm, V.; Panigrahi, S.C. Microstructural Investigations on As-Cast and Annealed Al–Sc and Al–Sc–Zr Alloys. Mater. Charact. 2009, *60*, 1387-1394. https://doi.org/10.1016/j.matchar.2009.06.012
34. Shi, C.; Zhang, L.; Wu, G.; Zhang, X.; Chen, A.; Tao, J. Effects of Sc Addition on the Microstructure and Mechanical Properties of Cast Al-3Li-1.5Cu-0.15Zr Alloy. *Mater. Sci. Eng. A* **2017**, *680*, 232-238. https://doi.org/10.1016/j.msea.2016.10.063
35. Liu, Y.; Zhang, C.C.; Zhang, X.Y.; Huang, Y.C. Understanding Grain Refinement of Sc Addition in a Zr Containing Al-Zn-Mg-Cu Aluminum Alloy from Experiments and First-Principles. *Intermetallics* **2020**, *123*, 106823. https://doi.org/10.1016/j.intermet.2020.106823
36. Pan, D.; Zhou, S.; Zhang, Z.; Li, M.; Wu, Y. Effects of Sc(Zr) on the Microstructure and Mechanical Properties of As-Cast Al–Mg Alloys. *Mater. Sci. Technol.* **2017**, *33*, 751-757. https://doi.org/10.1080/02670836.2016.1270573
37. Qin, J.; Tan, P.; Quan, X.; Liu, Z.; Yi, D.; Wang, B. The Effect of Sc Addition on Microstructure and Mechanical Properties of As-Cast Zr-Containing Al-Cu Alloys. *J. Alloys Compd*. **2022**, *909*, 164686. https://doi.org/10.1016/j.jallcom.2022.164686
38. Vlach, M.; Čížek, J.; Kodetová, V.; Kekule, T.; Lukáč, F.; Cieslar, M.; Kudrnová, H.; Bajtošová, L.; Leibner, M.; Harcuba, P.; Málek, J.; Neubert, V. Annealing Effects in Cast Commercial Aluminium Al–Mg–Zn–Cu(–Sc–Zr) Alloys. *Met. Mater. Int*. **2021**, *27*, 995-1004. https://doi.org/10.1007/s12540-019-00499-6
39. Toropova, L.S.; Eskin, D.G.; Kharakterova, M.L.; Dobatkina, T.V. *Advanced Aluminum Alloys Containing Scandium: Structure and Properties*; Routledge: London, UK, 1998; 188p. https://doi.org/10.4324/9781315097541
40. Watanabe, C.; Watanabe, D.; Monzen, R. Coarsening Behavior of Al_3Sc Precipitates in an Al–Mg–Sc Alloy. *Mater. Trans.* **2006**, *47*, 2285-2291. https://doi.org/10.2320/matertrans.47.2285
41. Forbord, B.; Hallem, H.; Røyset, J.; Marthinsen, K. Thermal Stability of $Al_3(Sc_x,Zr_{1-x})$-Dispersoids in Extruded Aluminium Alloys. *Mater. Sci. Eng. A* **2008**, *475*, 241-248. https://doi.org/10.1016/j.msea.2007.04.054
42. Vandersluis, E.; Lombardi, A.; Ravindran, C.; Bois-Brochu, A.; Chiesa, F.; MacKay, R. Factors Influencing Thermal Conductivity and Mechanical Properties in 319 Al Alloy Cylinder Heads. *Mater. Sci. Eng. A* **2015**, *648*, 401-411. https://doi.org/10.1016/j.msea.2015.09.091
43. Liu, Y.; Liu, Y.; Akhtar, S.; Wang, P.; He, Z.; Jiao, X.; Ge, S.; Yuan, G.; Zhang, Y.; Li, X.; Xiong S. Thermal Conductivity of Binary Al Alloys with Different Alloying Elements. *J. Alloys Compd*. **2025**, *1010*, 177257. https://doi.org/10.1016/j.jallcom.2024.177257
44. Zhang, A.; Li, Y. Effect of Alloying Elements on Thermal Conductivity of Aluminum. *J. Mater. Res.* **2023**, *38*, 2049-2058. https://doi.org/10.1557/s43578-023-00942-w
45. Guan, R.; Shen, Y.; Zhao, Z.; Wang, X. A High-Strength, Ductile Al-0.35Sc-0.2Zr Alloy with Good Electrical Conductivity Strengthened by Coherent Nanosized-Precipitates. *J. Mater. Sci. Technol*. **2017**, *33*, 215-223. https://doi.org/10.1016/j.jmst.2017.01.017
46. Yang, J.; Zhang, K.; Li, M.; Wang, S.; Chen, X. Effect of Zr Addition on the Microstructure and Mechanical Properties of As-Cast Al-Mg-Mn-Sc Alloys. *Int. J. Metalcast*. **2025**, *19*, 2881-2892. https://doi.org/10.1007/s40962-024-01510-6
47. Fuller, C.B.; Murray, J.L.; Seidman, D.N. Temporal Evolution of the Nanostructure of Al(Sc,Zr) Alloys: Part I – Chemical Compositions of $Al_3(Sc_{1-x}Zr_x)$ Precipitates. *Acta Mater*. **2005**, *53*, 5401-5413. https://doi.org/10.1016/j.actamat.2005.08.016
48. Seo, D.W.; Kim, J.H.; Lee, M.H.; Lee, S.H. Microstructure and Corrosion Characteristics According to the Si Content of Al-Ca-Si Alloys. *Sci. Adv. Mater.* **2022**, *14*, 1249-1257. https://doi.org/10.1166/sam.2022.4311
49. Cavanaugh, M.K.; Birbilis, N.; Buchheit, R.G.; Bovard, F. Investigating Localized Corrosion Susceptibility Arising from Sc Containing Intermetallic Al_3Sc in High Strength Al-Alloys. *Scr. Mater.* **2007**, *56*, 995-998. https://doi.org/10.1016/j.scriptamat.2007.01.036
50. Wloka, J.; Virtanen, S. Influence of Scandium on the Pitting Behaviour of Al–Zn–Mg–Cu Alloys. Acta Mater. 2007, *55*, 6666-6672. https://doi.org/10.1016/j.actamat.2007.08.021

 doi:10.20944/preprints202512.0932.v1

51. Ma, Y.; Liu, Y.; Wang, M. Microstructures and Corrosion Resistances of Hypoeutectic Al-6.5Si-0.45Mg Casting Alloy with Addition of Sc and Zr. *Mater. Chem. Phys.* **2022**, *276*, 125321. https://doi.org/10.1016/j.matchemphys.2021.125321
52. Kozlova, N.A.; Nokhrin, A.V.; Chuvil'deev, V.N.; Shandria, Y.S.; Bobrov, A.A.; Chegurov, M.K. The Effect of Sc:Zr Ratio on the Corrosion Resistance of Cast Al–Mg Alloys. *Phys. Met. Metallogr*. **2024**, *125*, 851-861. https://doi.org/10.1134/S0031918X24601550
53. Mondolfo, L.F. *Aluminum Alloys: Structure and Properties*; Butterworth-Heinemann: London, UK, 1976; 971p.